Vertical Wind Disturbances during a Strong Wind Event Observed by the PANSY Radar at Syowa Station, Antarctica

YOSHIHIRO TOMIKAWA

National Institute of Polar Research and The Graduate University for Advanced Studies (SOKENDAI), Tokyo, Japan

MASAHIRO NOMOTO AND HIROAKI MIURA

The University of Tokyo, Tokyo, Japan

MASAKI TSUTSUMI, KOJI NISHIMURA, TAKUJI NAKAMURA, HISAO YAMAGISHI, AND TAKASHI YAMANOUCHI

National Institute of Polar Research and The Graduate University for Advanced Studies (SOKENDAI), Tokyo, Japan

TORU SATO

Kyoto University, Kyoto, Japan

KAORU SATO

The University of Tokyo, Tokyo, Japan

(Manuscript received 5 September 2014, in final form 30 January 2015)

ABSTRACT

Characteristically strong vertical wind disturbances (VWDs) with magnitudes larger than 1 m s^{-1} were observed in the Antarctic troposphere using a new mesosphere–stratosphere–troposphere (MST) radar called the Program of the Antarctic Syowa MST/incoherent scatter (IS) Radar (PANSY) during 15–19 June 2012 at Syowa Station (69.0°S, 39.6°E). In the same period, two synoptic-scale cyclones approached Syowa Station and caused a strong wind event (SWE) at the surface. The VWDs observed during the SWE at Syowa Station had a nearly standing (i.e., no phase tilt with height) phase structure up to the tropopause and a power spectrum proportional to the $-5/3$ power of frequency. On the other hand, the observed VWDs were not associated with systematic horizontal momentum fluxes. Meteorological fields around Syowa Station during the SWE were successfully simulated using the Nonhydrostatic Icosahedral Atmospheric Model (NICAM). A strong VWD was also simulated at the model grid of 70.0°S, 40.0°E in NICAM, which had a standing phase structure similar to the observed ones. An analysis based on the Froude number showed that the simulated VWD was likely due to a hydraulic jump leeward of the coastal mountain ridge. The Scorer parameter analysis indicated that the observed VWDs at Syowa Station during 16–17 June 2012 were likely due to the hydraulic jump similar to that in NICAM. On the other hand, a possibility of lee waves was also suggested for the VWD observed on 18 June 2012.

1. Introduction

The Antarctic coastal region is characterized by strong surface winds throughout the year. These strong winds are primarily induced by the katabatic forcing due to the Antarctic topography (Parish and Bromwich 1987) and partially by synoptic-scale cyclones arriving from the Southern Ocean storm track (Trenberth 1991). The surface wind induced by the katabatic forcing is called ''katabatic wind'' and characterized by a nearly constant wind direction (King and Turner 1997). Among them, cases with strong surface winds, which are classified as gale winds (i.e., 17.2–20.7 m s^{-1}) or higher classes in the Beaufort Wind Force Levels are called strong wind events (SWEs) and have been intensively studied

Corresponding author address: Yoshihiro Tomikawa, National Institute of Polar Research, 10-3, Midori-cho, Tachikawa, Tokyo 190-8518, Japan.
E-mail: tomikawa@nipr.ac.jp

DOI: 10.1175/MWR-D-14-00289.1

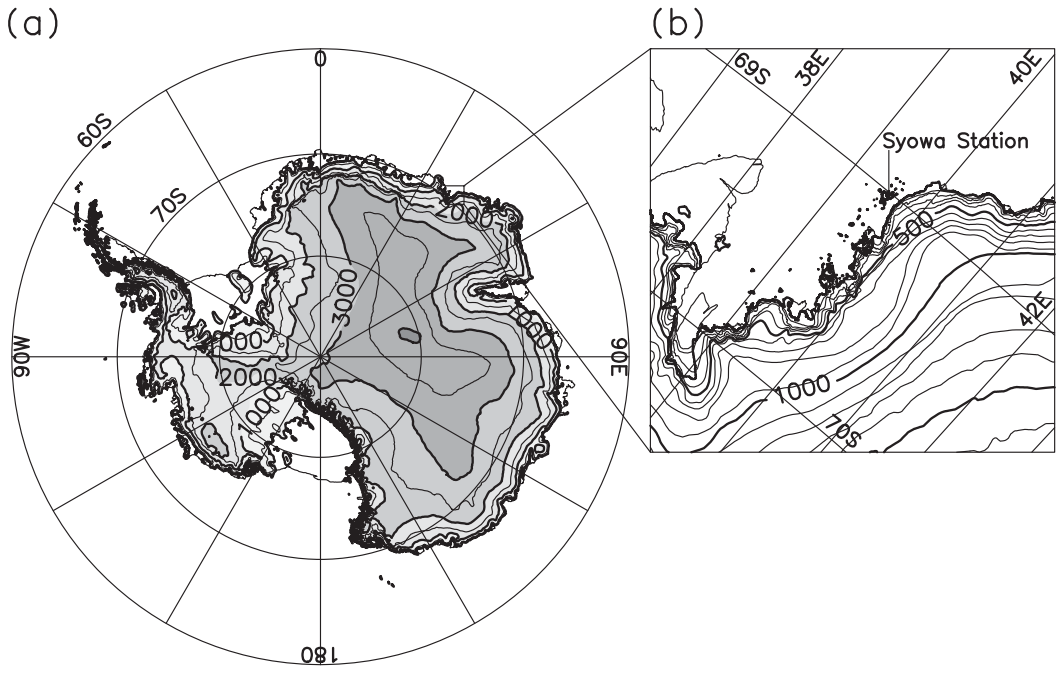

FIG. 1. (a) Antarctic topography with contour intervals of 500 m. (b) Inset of (a) showing the coastal region around Syowa Station with contour intervals of 100 m.

(Turner et al. 2009). Turner et al. (2001) examined an extreme wind event at Casey Station (66.27°S, 110.53°E) and concluded that key factors forcing the extreme wind were a synoptic-scale strong pressure gradient, entrainment of radiatively cooled air, topographically induced downslope wind, and sources of negative buoyancy. Steinhoff et al. (2008) examined a severe wind event at McMurdo Station (77.85°S, 166.67°E) and demonstrated that a barrier effect due to the Transantarctic Mountains played a significant role in forcing the strong surface wind in addition to the factors proposed by Turner et al. (2001).

These strong surface winds during SWEs cause several kinds of mesoscale phenomena such as hydraulic jumps, downslope windstorms, and lee waves by interacting with local topography in the Antarctic coastal region. Adams (2004) simulated an extreme wind event at Casey Station and suggested an occurrence of a hydraulic jump on the upslope from Casey Station. Steinhoff et al. (2008) indicated that a downslope windstorm also contributed to the enhancement of surface winds at McMurdo Station in the severe wind event. On the other hand, it is difficult to directly observe these mesoscale phenomena in the Antarctic because meteorological observations in the Antarctic are sparse compared to other areas.

Valkonen et al. (2010) and Arnault and Kirkwood (2012) observed vertical wind disturbances (VWDs) in the troposphere and lower stratosphere at Finnish/Swedish Aboa/Wasa Station (73.0°S, 13.4°W) with the Moveable Atmospheric Radar for Antarctica (MARA). They simulated the VWDs with the Weather Research and Forecasting (WRF) Model and demonstrated that the VWDs were induced by topographically forced gravity waves (i.e., mountain waves). It is also shown that those gravity waves propagated up to the lower stratosphere under a condition of weak zonal wind shear. However, these observations of mesoscale phenomena in the Antarctic troposphere and lower stratosphere are still limited.

Syowa Station (69.0°S, 39.6°E) is a primary station of the Japanese Antarctic activity and located on East Ongul Island in the Antarctic coastal region (Fig. 1). Japanese Antarctic Research Expeditions (JAREs) have been performing operational meteorological observations at Syowa Station since 1957 (e.g., Sato and Hirasawa 2007). In addition, the first mesosphere–stratosphere–troposphere (MST)/incoherent scatter (IS) radar in the Antarctic has been installed at Syowa Station (Sato et al. 2014), which is called the Program of the Antarctic Syowa MST/IS Radar (PANSY). The PANSY radar has the ability to make continuous measurements of vertical profiles of zonal, meridional, and vertical winds with fine vertical and temporal resolutions regardless of the weather conditions. The radar has started its continuous observation of the troposphere and stratosphere on 30 April 2012.

In June 2012 when an SWE occurred at Syowa Station, intense vertical wind disturbances in the troposphere were observed by the PANSY radar.

The primary purpose of this study is to examine what mechanism caused the observed VWDs using observational data and performing a model simulation. Data and model settings used in this study are given in section 2. Synoptic-scale meteorological fields during the SWE around Syowa Station are shown in section 3. The characteristics of the VWDs observed by the PANSY radar are described in section 4. Simulated VWDs and their characteristics are compared with observed ones in section 5. A mechanism causing the simulated and observed VWDs is examined in section 6. The summary and conclusions are given in section 7.

2. Observation and model configuration

a. Observational data

The PANSY radar is a VHF clear-air Doppler radar operating at its central frequency of 47.0 MHz. The PANSY radar measurements were made by using five beams pointing vertically and to the north, east, south, and west with a zenith angle of 10° in the troposphere and lower stratosphere. Line-of-sight wind velocities are estimated from Doppler frequency shifts in the echoes with a high accuracy of 0.1 m s^{-1}. The radar has an advantage in directly being able to measure vertical winds, which are important to examine secondary circulations of weather systems and vertical fluxes of horizontal momentum. The vertical resolution is 150 m for the troposphere and stratosphere. A continuous observation using a reduced radar system composed of 228 crossed Yagi antennas has started on 30 April 2012. The time resolution is 1 min before 25 June 2012 and 2 min after that. See Sato et al. (2014) for details of the PANSY radar system.

Operational meteorological observations have been performed at Syowa Station since 1957. Surface meteorological parameters such as horizontal wind (10 min averaged) and temperature are obtained at a time interval of 1 h. Radiosonde observations are made to obtain vertical profiles of temperature, horizontal wind, and humidity twice a day. Thermal tropopauses are determined from the temperature profiles based on the World Meteorological Organization's definition: the lowest level at which the lapse rate decreases to 2°C km^{-1} or less, provided also the average lapse rate between this level and all higher levels within 2 km does not exceed 2°C km^{-1} (WMO 1957).

To examine the synoptic-scale atmospheric fields (i.e., cyclones), infrared satellite images taken by Advanced Very High Resolution Radiometer (AVHRR) on board *NOAA-16* and reanalysis data from Modern-Era Retrospective Analysis for Research and Applications (MERRA; Rienecker et al. 2011) are used. AVHRR data were received at Syowa Station and provided by the National Institute of Polar Research (NIPR). Cyclone tracks are determined as series of the locations of sea level pressure (SLP) minima.

b. Numerical simulation

We carried out a numerical simulation to examine the atmospheric fields around Syowa Station during the SWE. The Nonhydrostatic Icosahedral Atmospheric Model (NICAM; Satoh et al. 2008) was used to simulate the synoptic-scale cyclones over the ocean and strong VWDs in the Antarctic coastal region.

This model employs nonhydrostatic dynamical cores as the governing equations, and icosahedral grids over the sphere. The finite-volume method is used for numerical discretization to conserve total mass, momentum, and energy over the domain. Horizontal resolutions are represented by "glevel-n" (grid division level n). Glevel-0 means the original icosahedron. By recursively dividing each triangle into four small triangles, we obtain one-level higher resolution. Moreover, NICAM can define grids that are finer in the target region by using the grid transformation method proposed by Tomita (2008a). The stretching factor β represents the ratio between maximum and minimum grid intervals. Stretched grids involve less computational cost than quasi-uniform grids for regional climates or weather studies. Note that this model does not have lateral boundaries and, hence, it is free from the artificial wave reflection from the boundaries unlike regional models.

Most previous studies using NICAM have focused on atmospheric phenomena in the tropics. Miura et al. (2007) simulated the Madden–Julian oscillation (MJO) with glevel-11 (Δx = 3.5 km) on the Earth Simulator. Fudeyasu et al. (2008) simulated two real tropical cyclone life cycles over 1–2 weeks after initialization. We are the first to apply NICAM to the phenomena in the polar region.

The model settings we used in this study are described in what follows. The horizontal grid was set at glevel-8 with β = 100 centered at 65°S, 15°E (to the west of Syowa Station), as shown in Fig. 2a. This grid configuration enables better simulation of cyclones developing to the west (upstream) of Syowa Station. The grid intervals were about 2.8 km at the center, about 280 km at its antipodal point, and about 5 km near Syowa Station (Fig. 2b). The vertical grids were distributed at 80 levels with their spacing varying from 80 m (bottom) to 1.5 km (top: 40-km altitude). The time step was 15 s. NICAM Single-moment Water 6 scheme (NSW6; Tomita 2008b) was selected for the microphysics, based on Lin et al. (1983) who calculated six categories (i.e., water vapor, cloud

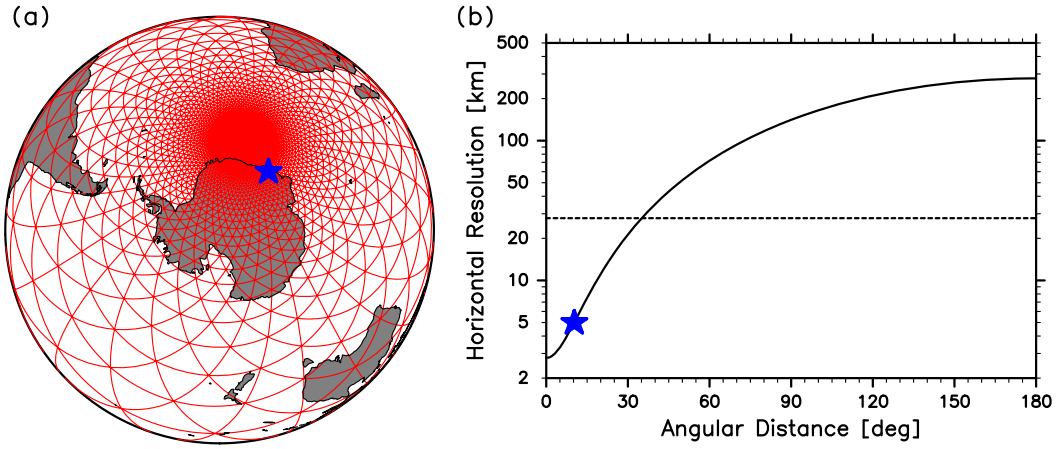

FIG. 2. (a) Illustration of stretched grid (16 times coarser than the simulation in this study). (b) Resolution distribution of stretched grid (solid) and quasi-uniform grid with the same number of grid points (dotted). Stars represent Syowa Station.

water, rain, cloud ice, snow, and graupel). The Mellor–Yamada–Nakanishi–Niino (MYNN) level 3 scheme (Nakanishi and Niino 2004) was used as the boundary layer scheme. A bucket model was used for the land surface model. A mixed layer model was used for the sea surface model. Parameterizations for cumulus convection and gravity wave forcing were not included because the grid spacing was sufficiently fine in the target region. The initial value was created using the National Centers for Environmental Prediction (NCEP) final operational global analysis (FNL) data at 0000 UTC 14 June 2012. Integration was performed over 120 h without assimilation (i.e., cold start). The NICAM data were output every 1 min. Daily SST data from NCEP-FNL and monthly-mean sea ice thickness data from the CMIP3 multimodel ensemble means were nudged with a relaxation time of 120 h.

3. Description of the strong wind event

Figure 3 shows the time series of surface wind speed, wind direction, and temperature obtained by operational meteorological observations at Syowa Station in

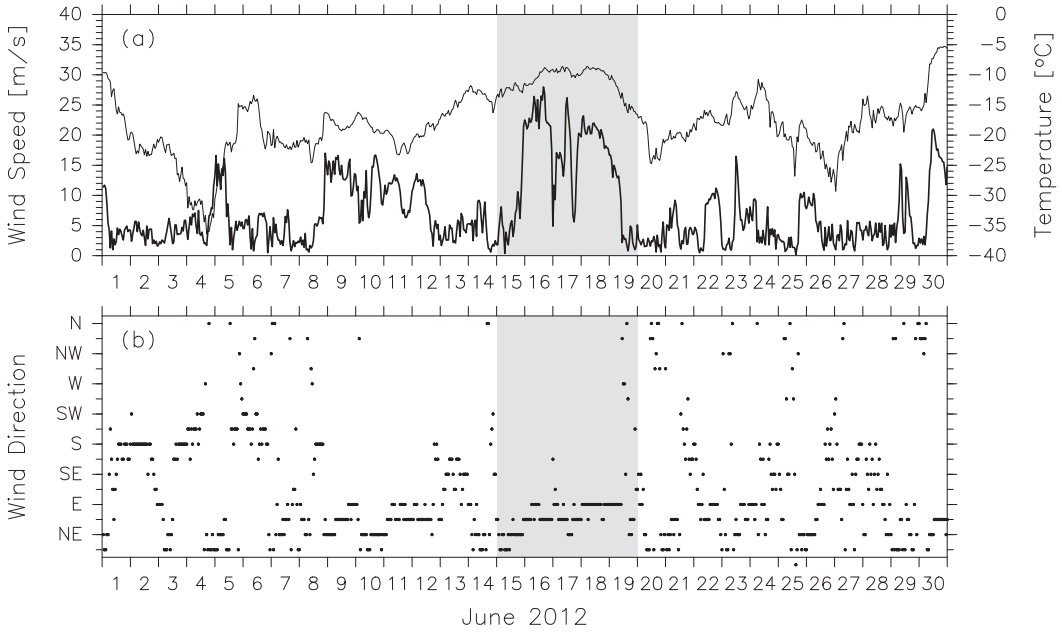

FIG. 3. Time variations of (a) (10-min averaged) surface wind speed (thick) and temperature (thin) and (b) direction of surface wind obtained by operational meteorological observations at Syowa Station in June 2012. A shaded area represents the period 15–19 Jun 2012.

June 2012. The surface wind speed shown by a thick solid line in Fig. 3a was often faster than 20 m s^{-1} during 15–19 June 2012. We define this period as an SWE and focus on it in this study. The period of 15–19 June 2012 is shaded in Fig. 3. The wind direction during the SWE was distributed between the northeast and east. This is a general feature of SWEs at Syowa Station (Sato and Hirasawa 2007). During the SWE, the surface temperature was higher than that in the weak wind period before and after the SWE. This feature is also common to other SWEs at Syowa Station. Thus, this SWE can be regarded as a typical one at Syowa Station.

During the SWE, two cyclones generated over the Southern Ocean approached Syowa Station and contributed to the enhancement of surface wind at Syowa Station. To describe their development and decay and their tracks, Fig. 4 shows a series of infrared satellite images taken by the AVHRR and SLP of MERRA during 14–18 June 2012. At 0900 UTC 14 June (3 h after the time shown in Fig. 4a), one cyclone (hereafter referred to as cyclone A) appeared at 61°S, 2°W (not shown), which was different from the cyclone seen at 63°S, 16°W in Fig. 4a. The track of cyclone A determined from its SLP minimum at each time is shown by a green line in Fig. 4. Cyclone A advanced eastward along 60°S and its SLP minimum reached 955 hPa at 0600 UTC 15 June (Fig. 4b). In the next 24 h, cyclone A moved toward Syowa Station while keeping its SLP minimum (Fig. 4c) and produced a large pressure gradient around Syowa Station. Another cyclone (hereafter cyclone B) was generated to the east of the southern Andes around 70°W and first observed at 57°S, 3°E at 0600 UTC 16 June (Fig. 4c). The track of cyclone B is shown by a red line in Fig. 4. Cyclone B advanced eastward and slightly poleward, and reached 60°S at 0600 UTC 17 June (Fig. 4d). At the same time, the SLP minimum of cyclone B decreased to 944 hPa. Cyclone B absorbed cyclone A by 1200 UTC 17 June (Fig. 4e) and advanced to 63°S, 42°E at 0600 UTC 18 June with a minimum SLP of 948 hPa (Fig. 4f). Development and movement of cyclone B toward Syowa Station further enhanced the pressure gradient around Syowa Station (Figs. 4d–f). Cyclone B left Syowa Station by 1200 UTC 19 June (not shown) and the SWE at Syowa Station also finished as shown in Fig. 3.

4. PANSY radar observations

Figure 5 shows time–altitude sections of zonal, meridional, and vertical winds below an altitude of 14 km observed by the PANSY radar in June 2012. The data are smoothed with a lowpass filter having a cutoff period of 3 h in time and a cutoff length of 1 km in the vertical. The top of the observed altitude region rose up to 20 km on 25 June because the time resolution changed from 1 to 2 min due to the change of pulse code length used in the observations. The altitude region below 1.5 km cannot be observed by the PANSY radar because of the transmitter/receiver switching. During the SWE in 15–19 June, the zonal wind in the troposphere was mainly easterly (Fig. 5a), which is consistent with the approach of two cyclones from the north. The meridional wind in the troposphere changed its direction from northerly to southerly (Fig. 5b). This is also consistent with the fact that cyclone B passed slightly north of Syowa Station on 18 June (Fig. 4f). On the other hand, the vertical wind exhibited strong disturbances with periods much shorter than dominant periods of zonal and meridional wind disturbances (i.e., several days) during the SWE (Fig. 5c).

To examine the VWDs during the SWE in more detail, a time–altitude section of unfiltered vertical wind in 16–18 June 2012 is shown in Fig. 6. It is found that the vertical wind had many disturbances with a wide frequency range. For example, the vertical wind showed a strong disturbance with a period of 1–2 h around 0000 UTC 17 June. On the other hand, the disturbance around 1200 UTC 17 June had a period of about 4 h. In addition, the phase of these VWDs seems almost standing (i.e., no phase tilt with height) in most cases. Another point to note is that the VWDs were deep but mostly confined below the thermal tropopause shown by crosses in Fig. 6.

Since the VWDs during the SWE had a wide frequency range, their power spectrum in a frequency range between (2 min)$^{-1}$ and (17 h)$^{-1}$ was computed by the Blackman–Tukey method (Blackman and Tukey 1958) at each altitude using the unfiltered vertical wind data in 16–18 June 2012. Available data with sufficiently high signal-to-noise ratio were over 90% for the vertical beam and 75% for oblique beams in the altitude region below 10 km (see Fig. 6). Figure 7 shows the power spectrum calculated using vertical wind fluctuations observed by the PANSY radar and averaged over an altitude region of 2–4 km during 16–18 June 2012. It is found that the power spectrum of vertical wind was roughly proportional to the $-5/3$ power of frequency (ω). Such a power spectrum proportional to $\omega^{-5/3}$ has been discovered in other VHF radar observations (Ecklund et al. 1985, 1986). Sato (1990) also obtained the power spectrum of vertical wind proportional to $\omega^{-5/3}$ with the middle and upper atmosphere (MU) radar observations at Shigaraki (34.9°N, 136.1°E), Japan, and demonstrated that such a spectral shape was likely due to phase modulations of topographically forced gravity waves in slowly varying background winds.

Vertical fluxes of zonal and meridional momentums were estimated by using the method of Vincent and

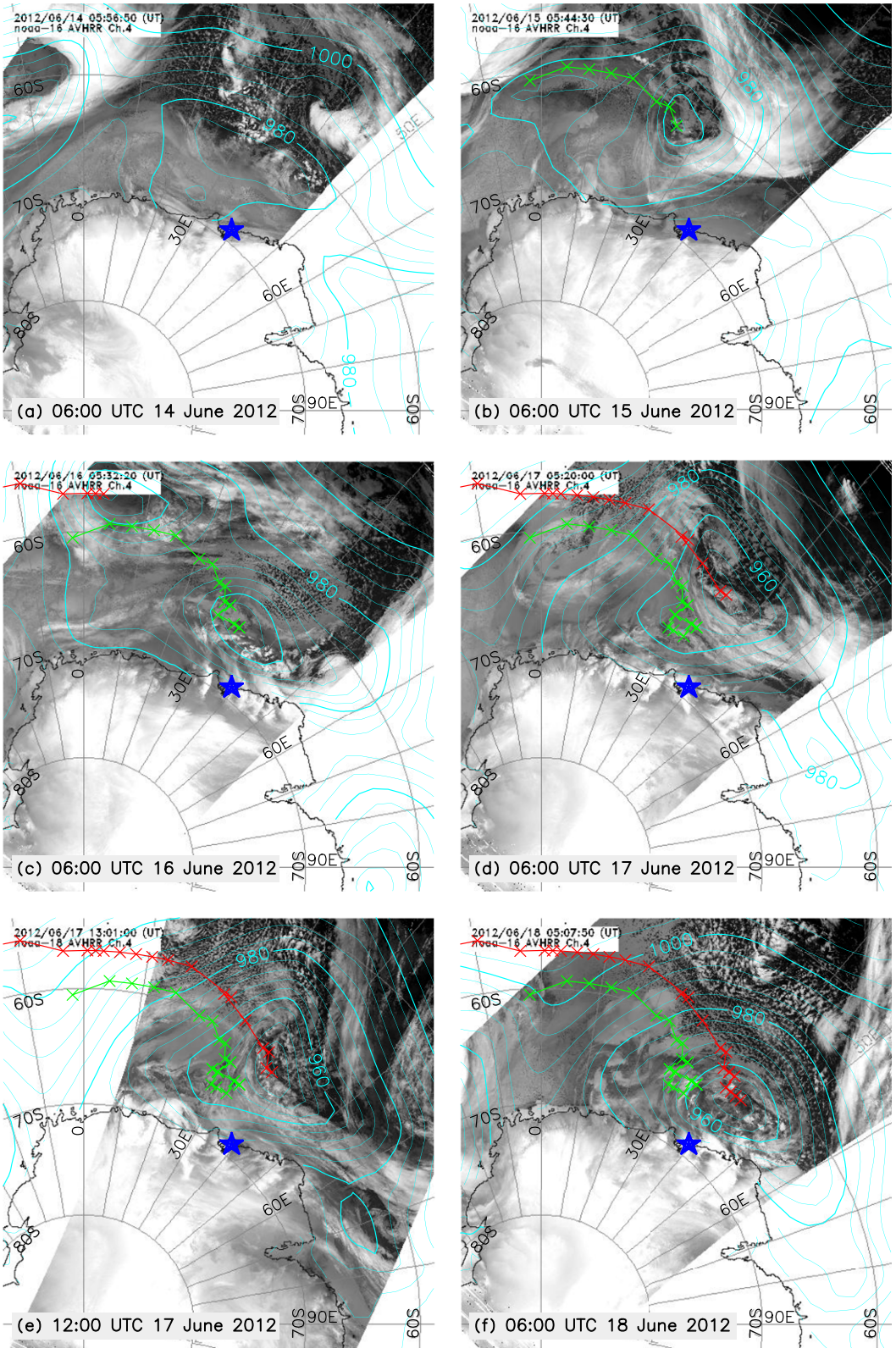

FIG. 4. AVHRR infrared satellite images and MERRA SLP (contours) at (a) 0600 UTC 14 Jun, (b) 0600 UTC 15 Jun, (c) 0600 UTC 16 Jun, (d) 0600 UTC 17 Jun, (e) 1200 UTC 17 Jun, and (f) 0600 UTC 18 Jun 2012. Contour intervals of SLP are 4 hPa. Green and red crisscrosses denote the tracks of cyclones A and B, respectively. Stars represent the location of Syowa Station.

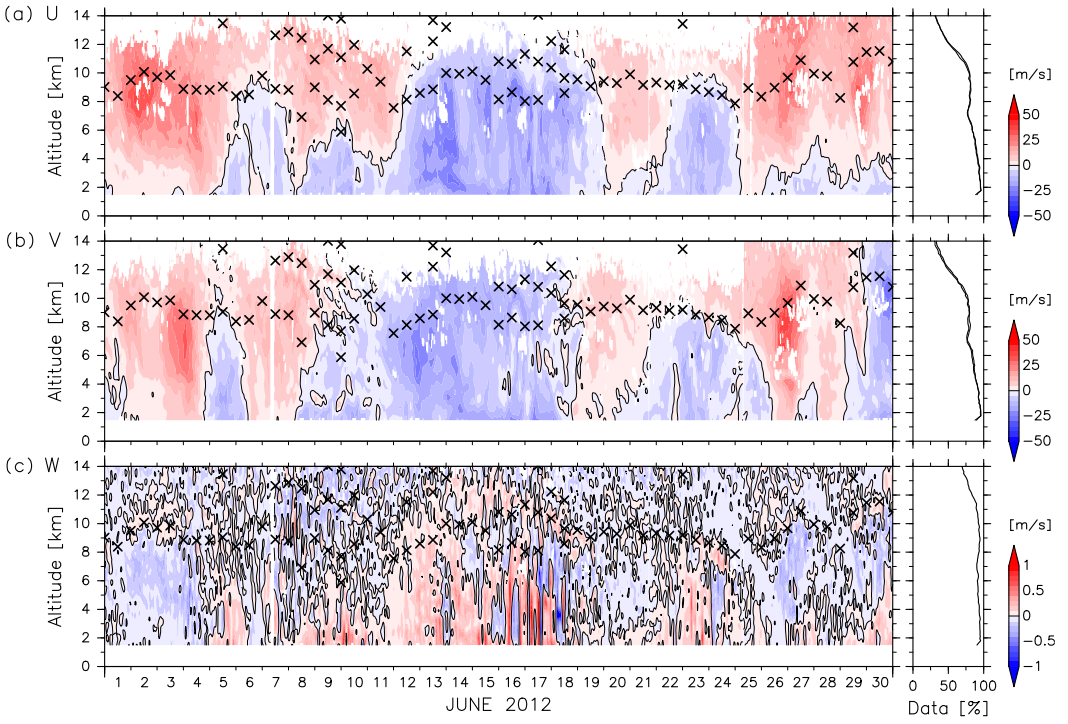

FIG. 5. Time–altitude sections of (a) zonal, (b) meridional, and (c) vertical winds observed by the PANSY radar in June 2012. Only the contours of 0 m s^{-1} are plotted. The data were smoothed by a lowpass filter with a cutoff period of 3 h in time and a cutoff length of 1 km in the vertical. Crisscrosses denote thermal tropopauses determined by radiosonde observations. The right panels show the fractions of available data for respective winds and altitudes.

Reid (1983) for the fluctuation components with periods shorter than 13 h, which was the inertial period at Syowa Station. The vertical fluxes of zonal momentum ($\overline{u'w'}$) and meridional momentum ($\overline{v'w'}$) and the variance of vertical wind ($\overline{w'^2}$) are shown in Fig. 8, where u', v', and w' are the zonal, meridional, and vertical wind fluctuation components, respectively, and overbars mean a lowpass filter with a cutoff period of 13 h. Large $\overline{w'^2}$ in the troposphere was observed around 0000 UTC 17 June, 1400 UTC 17 June, and 1200 UTC 18 June 2012, during which strong VWDs with a standing phase structure were observed in the unfiltered vertical

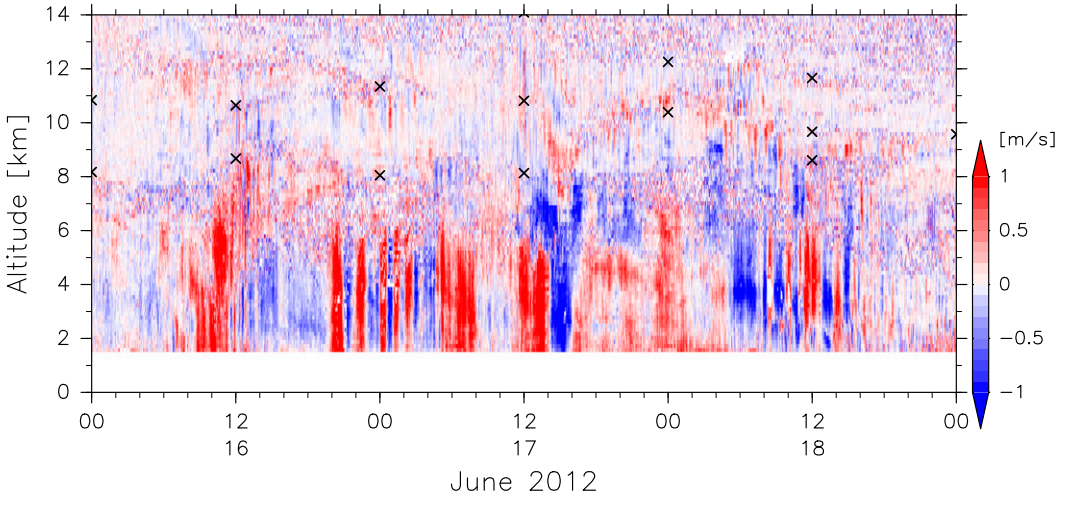

FIG. 6. As in Fig. 5, but for unfiltered vertical wind observed by the PANSY radar during 16–18 Jun 2012.

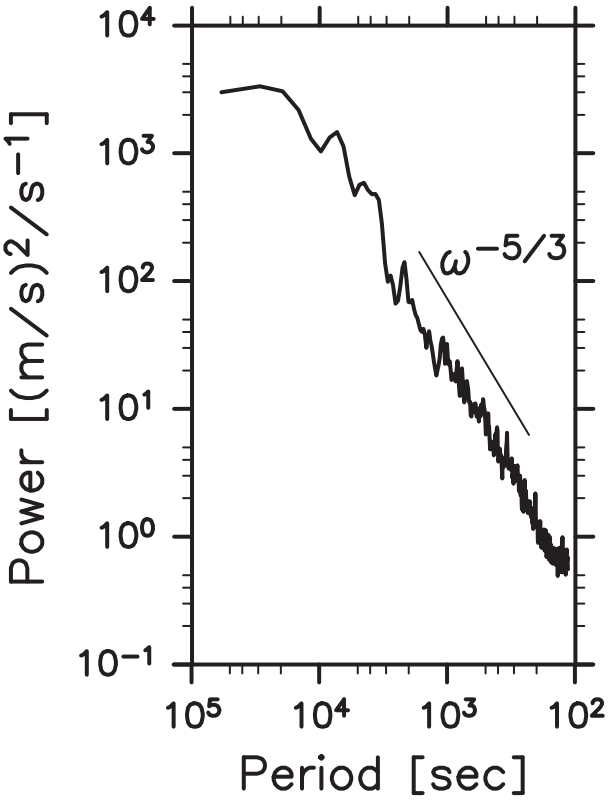

FIG. 7. Power spectrum calculated using vertical wind fluctuations observed by the PANSY radar and averaged over an altitude region of 2–4 km during 16–18 Jun 2012.

wind (see Fig. 6). In these periods, absolute values of $\overline{u'w'}$ and $\overline{v'w'}$ were not very large compared with those in the time periods before and after the VWDs. In contrast, a large negative $\overline{u'w'}$ was observed around 0600 UTC 17 June, in which $\overline{w'^2}$ was small.

5. Results of the NICAM simulation

In this section, meteorological fields around Syowa Station simulated by NICAM are compared with observations during 14–18 June 2012. First, cyclones simulated in NICAM are validated in comparison to satellite observations and MERRA. Figure 9 shows a series of outgoing longwave radiation (OLR) and SLP simulated by NICAM. Green and red lines represent the tracks of cyclones A and B, respectively, which were determined by their SLP minima.

Although the simulation was still in a spinup time at 0600 UTC 14 June (Fig. 9a), SLP fields and cloud distributions were well reproduced compared to the satellite observation (Fig. 4a). In the next 24 h, cyclone A appeared and moved to 60°S, 26°E at 0600 UTC 15 June (Fig. 9b). Cyclone A advanced to 61°S, 47°E at 0600 UTC 16 June (Fig. 9c), which was located to the east of cyclone A in AVHRR data by 10° (Fig. 4c). Cyclone B moved from 57°S, 11°E at 0600 UTC 16 June (Fig. 9c) to 59°S, 37°E at 0600 UTC 17 June (Fig. 9d) with a significant SLP depression from 950 to 934 hPa, which is lower than the observed. One reason for the larger SLP depression in NICAM may be insufficient horizontal resolution (not shown). By this time, cyclone B absorbed cyclone A, and then advanced to 61°S, 43°E at 1200 UTC 17 June (Fig. 9e). Although this location is slightly to the east of cyclone B observed in AVHRR data (Fig. 4e), cyclone B simulated by NICAM produced a similar distribution of large pressure gradient around Syowa Station. Later, simulated cyclone B decayed by 0600 UTC 18 June more quickly than that in AVHRR data (Fig. 9f).

Figure 10 shows time–altitude sections of respective wind components and temperature obtained by the PANSY radar and radiosonde observations at Syowa Station, and those of NICAM at Syowa Station and 70.0°S, 40.0°E during 14–18 June 2012. The model grid at 70.0°S, 40.0°E is located to the south of Syowa Station by 120 km. The PANSY radar data were smoothed with a lowpass filter having a cutoff period of 3 h. All the zonal wind distributions showed that easterly wind was dominant in the troposphere throughout the period (Figs. 10a,e,i). Meridional wind distributions also exhibited a common feature that the northerly wind in the troposphere was weaker in the second half period than in the first half (Figs. 10b,f,j). The tropopause altitude determined by each temperature profile was higher in NICAM than in the observations during 16–17 June. It is because strong temperature inversion at 9–10 km is designated as the tropopause in the observations (Fig. 10d), which is weaker in the NICAM temperature distributions (Figs. 10h,l). Thus, it can be considered that synoptic-scale meteorological fields around Syowa Station during 14–18 June 2012 were well reproduced by NICAM.

On the other hand, there was a clear difference between observed and simulated vertical wind distributions. Compared with the observed vertical wind characteristics in the troposphere during 16–18 June (Fig. 10c, and see also Fig. 6), the disturbances in simulated vertical winds at Syowa Station and 70.0°S, 40.0°E are relatively weaker and the dominant periods are longer in the troposphere except for the time period around 0000 UTC 16 June at 70.0°S, 40.0°E (Fig. 10k). The VWD around 0000 UTC 16 June at 70.0°S, 40.0°E had a nearly standing phase structure and a period of about 6 h. Although its period was longer than those of observed VWDs, its vertical structure was similar to the observed ones.

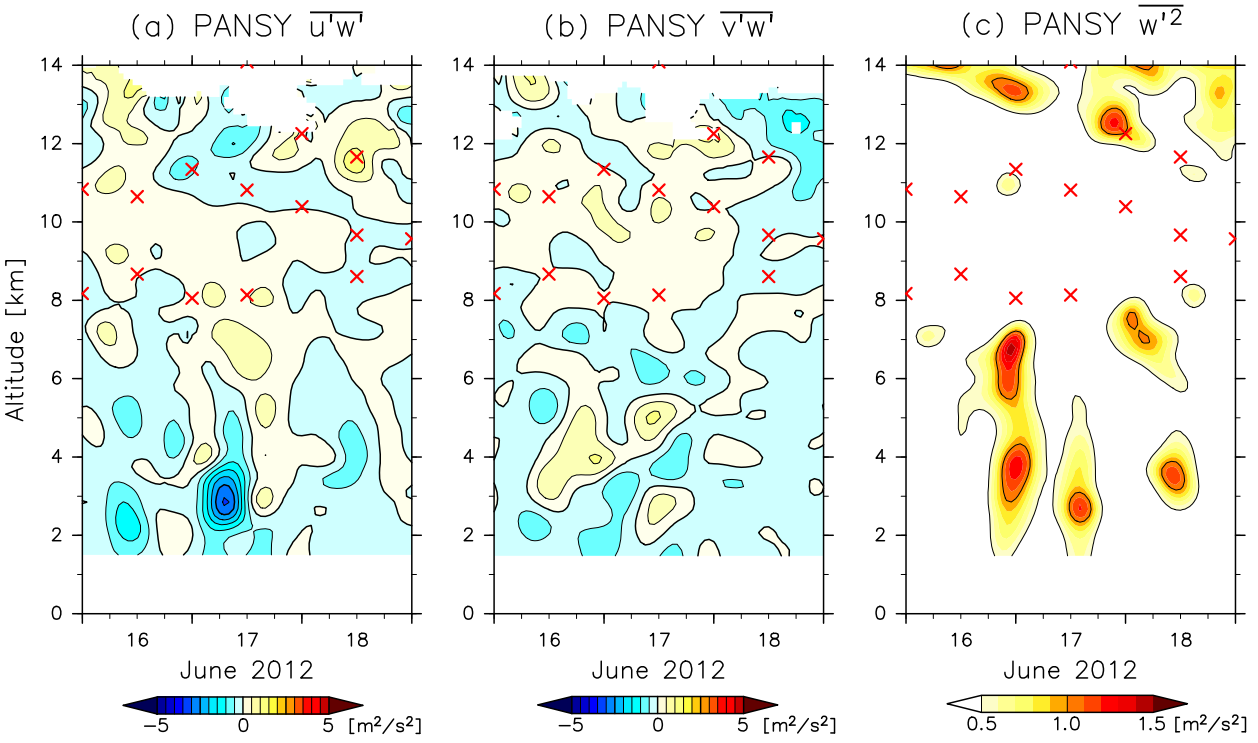

FIG. 8. Time–altitude sections of vertical fluxes of (a) zonal and (b) meridional momentums and (c) variances of vertical wind observed by the PANSY radar. Crisscrosses denote thermal tropopauses.

As shown in Fig. 10, the VWDs appeared at slightly different times and locations between the observations and NICAM. To compare the observed and simulated near-surface winds, Fig. 11 shows a time series of near-surface wind speeds and wind directions observed at Syowa Station and simulated at Syowa Station and 70.0°S, 40.0°E in NICAM. While the observed winds at the surface and at an altitude of 120 m are very similar both in their speed and direction, the simulated winds at the lowest and second lowest model levels (i.e., altitudes of 40 and 120 m, respectively) exhibited a large vertical wind shear both at Syowa Station and 70.0°S, 40.0°E. The simulated winds at the lowest model level hardly exceed 10 m s^{-1} throughout the period unlike the surface winds observed at Syowa Station, which may be due to the physical parameterizations in the boundary layer of NICAM. The wind speeds and directions observed at an altitude of 120 m above Syowa Station are similar to those at 70.0°S, 40.0°E in NICAM except for later enhancement of wind speed around 1800 UTC 15 June and a weaker wind speed by about 10 m s^{-1}. On the other hand, the simulated winds at Syowa Station in NICAM did not reproduce temporal variations of wind speed observed at Syowa Station. Such a difference between the observations and NICAM might be due to the fact that cyclone A in NICAM passed off the coast of Syowa Station earlier than in the observations (see Figs. 4 and 9). Thus, it can be considered that NICAM simulated VWDs around Syowa Station somewhat similar to those observed.

To compare spectral features between simulated and observed vertical winds, the power spectrum of simulated vertical winds in a time period from 0600 UTC 15 June to 1200 UTC 16 June at 70.0°S, 40.0°E is shown in Fig. 12. For comparison, the power spectrum obtained by the PANSY radar observation (i.e., shown in Fig. 7) is also plotted. It is found that the averaged power spectrum of simulated vertical wind in an altitude region of 2–4 km was almost proportional to ω^{-6}. This result indicates that the VWDs in NICAM were significantly suppressed compared to those in the PANSY radar observations in a higher-frequency range. One possible reason for such a difference is the narrow beamwidth of the PANSY radar. The reduced system of the PANSY radar used for the observations in June 2012 had a two-way beamwidth of about 5° (Sato et al. 2014), which is corresponding to a horizontal resolution of 0.4–0.5 km at an altitude of 5 km. Since the horizontal resolution of NICAM used in this study was about 5 km around Syowa Station, it is likely that the PANSY radar observations captured VWDs with smaller horizontal scales than in NICAM.

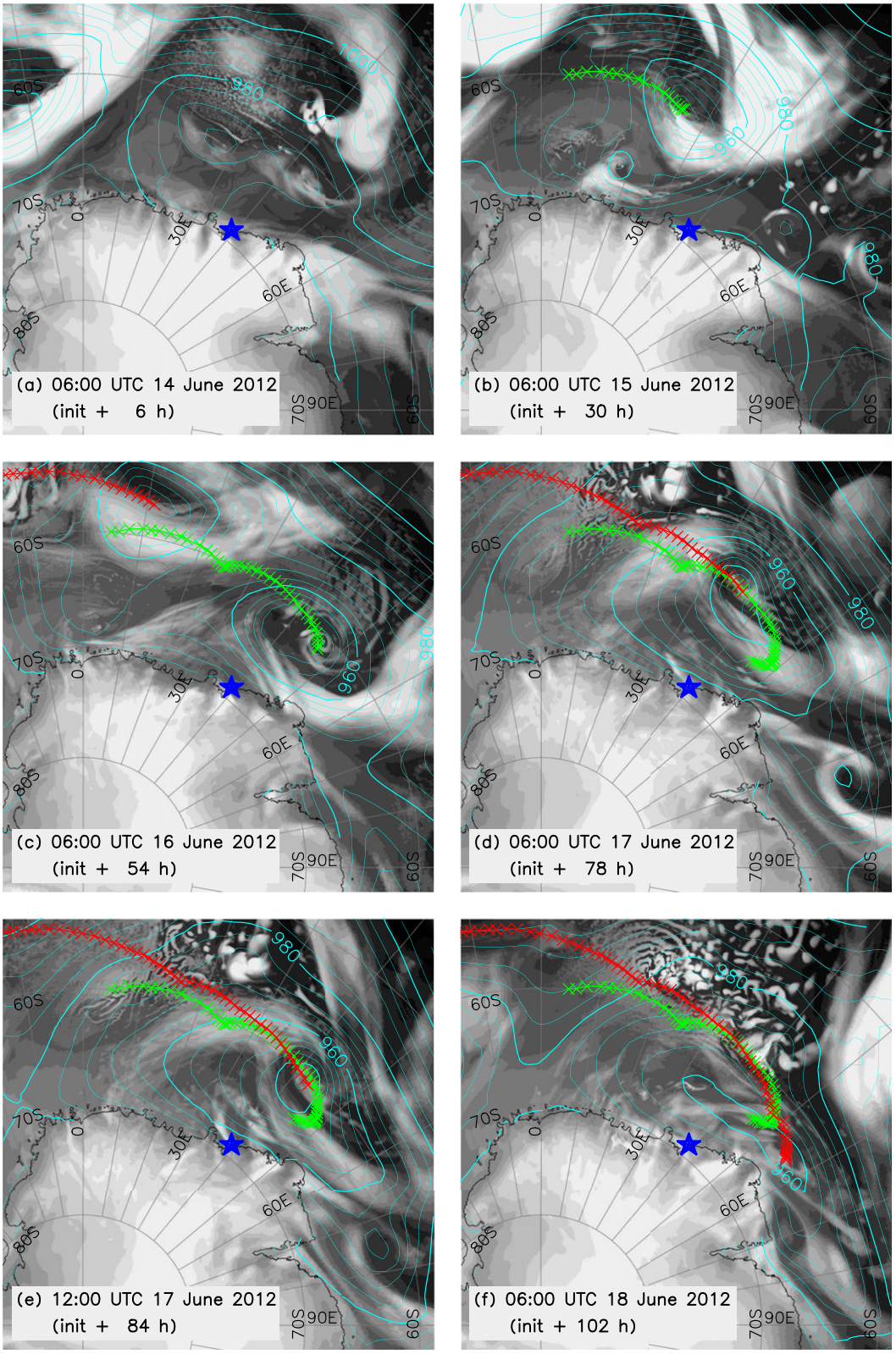

FIG. 9. As in Fig. 4, but for OLR images and SLP simulated by NICAM.

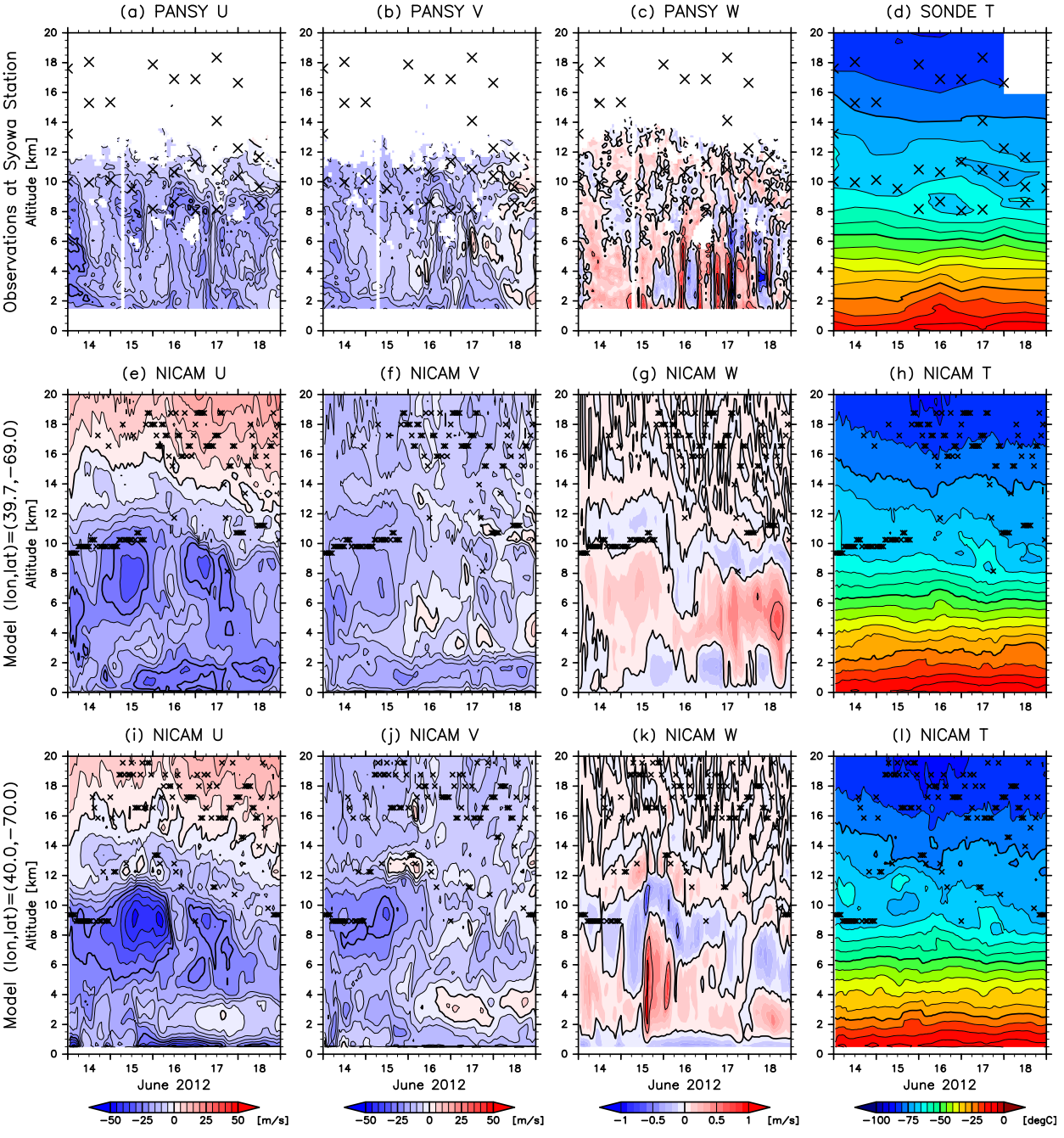

FIG. 10. Time–altitude sections of (a),(e),(i) zonal winds; (b),(f),(j) meridional winds; (c),(g),(k) vertical winds; and (d),(h),(l) temperature. (a)–(d) Observational data at Syowa Station and data simulated by NICAM at (e)–(h) Syowa Station and (i)–(l) 70.0°S, 40.0°E. Contour intervals are 5 m s^{-1} for zonal and meridional winds, 0.1 m s^{-1} for vertical winds, and 5°C for temperature. Crisscrosses denote thermal tropopauses.

Figure 13 shows time–altitude sections of the vertical fluxes of zonal momentum ($\overline{u'w'}$) and meridional momentum ($\overline{v'w'}$) and the variance of vertical wind ($\overline{w'^2}$) at 70.0°S, 40.0°E computed by the NICAM data. As in Fig. 8, the overbars signify a lowpass filter with a cutoff period of 13 h. All of them were clearly smaller than observed ones by one order of magnitude (see Fig. 8). The ratios of horizontal momentum fluxes relative to the variance of vertical wind (i.e., $|\overline{u'w'}|/\overline{w'^2}$ and $|\overline{v'w'}|/\overline{w'^2}$) were as much as 5–10, which are larger than 2–3 for the observed VWDs (Fig. 8). In addition, both of $\overline{u'w'}$ and $\overline{v'w'}$ exhibited a wavy structure in the vertical unlike

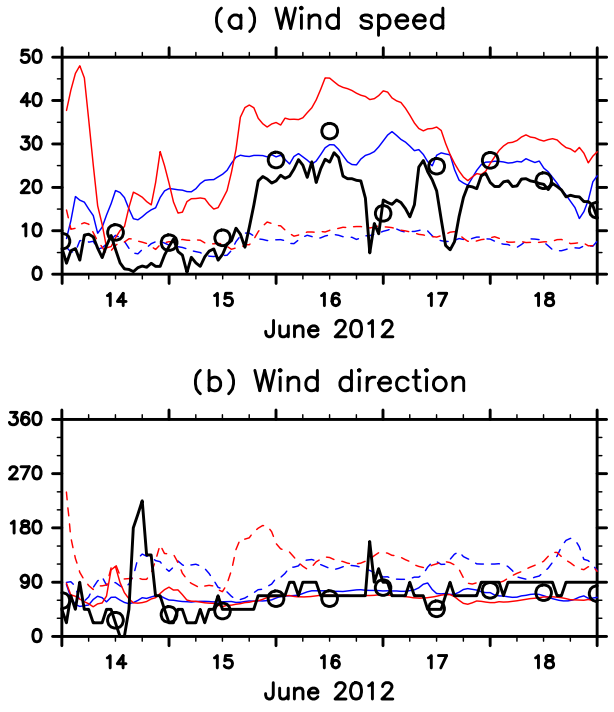

FIG. 11. Time series of (a) near-surface wind speeds and (b) wind directions. Black lines represent surface winds at Syowa Station obtained by the operational meteorological observations. Black circles represent winds at an altitude of 120 m at Syowa Station obtained by the radiosonde observations. Blue and red lines represent winds at Syowa and 70°S, 40°E in NICAM, respectively, at altitudes of 40 (dashed) and 120 m (solid).

those for the observed VWDs. These features may be due to fluctuations with a period close to the cutoff period of 13 h, because the higher-frequency components of VWDs in NICAM were much weaker than in the observations. We further examine the simulated VWD around 0000 UTC 16 June at 70.0°S, 40.0°E in the next section.

6. Dynamics of the VWDs

Figure 14 shows horizontal distributions of simulated vertical winds and horizontal wind vectors at an altitude of 5 km around Syowa Station at 1400 UTC 15 June 2012, when the strong VWD was seen at 70.0°S, 40.0°E in NICAM. Topography around Syowa Station is given by solid contours. While the coastline and altitude contours mostly extended from northeast to southwest, several mountain ridges and troughs nearly perpendicular to the coastline were located over the continent. There was a strong upward wind region perpendicular to the horizontal wind around 70.0°S, 40.0°E, which was located leeward of the coastal mountain ridge shown by curve A in Fig. 14. Another upward wind region was observed

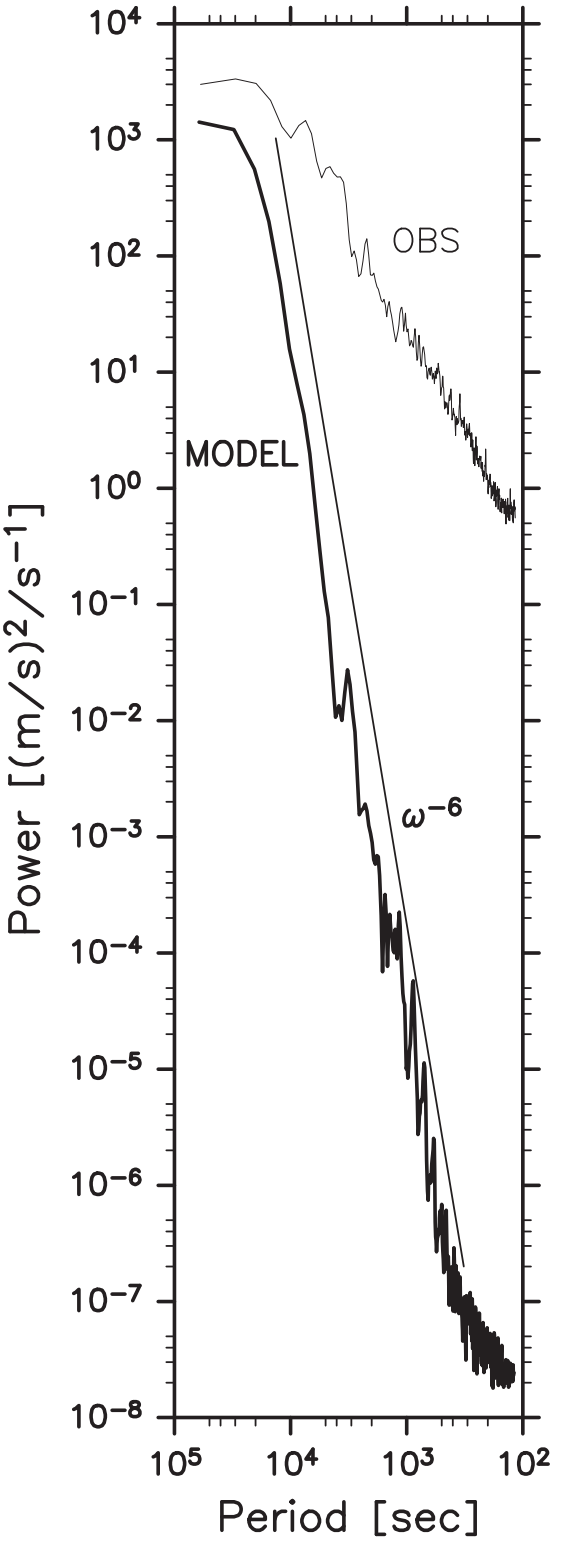

FIG. 12. As in Fig. 7, but for the NICAM data at 70.0°S, 40.0°E from 0600 UTC 15 Jun to 1200 UTC 16 Jun 2012. The power spectrum of the PANSY radar data (i.e., Fig. 7) is plotted for comparison.

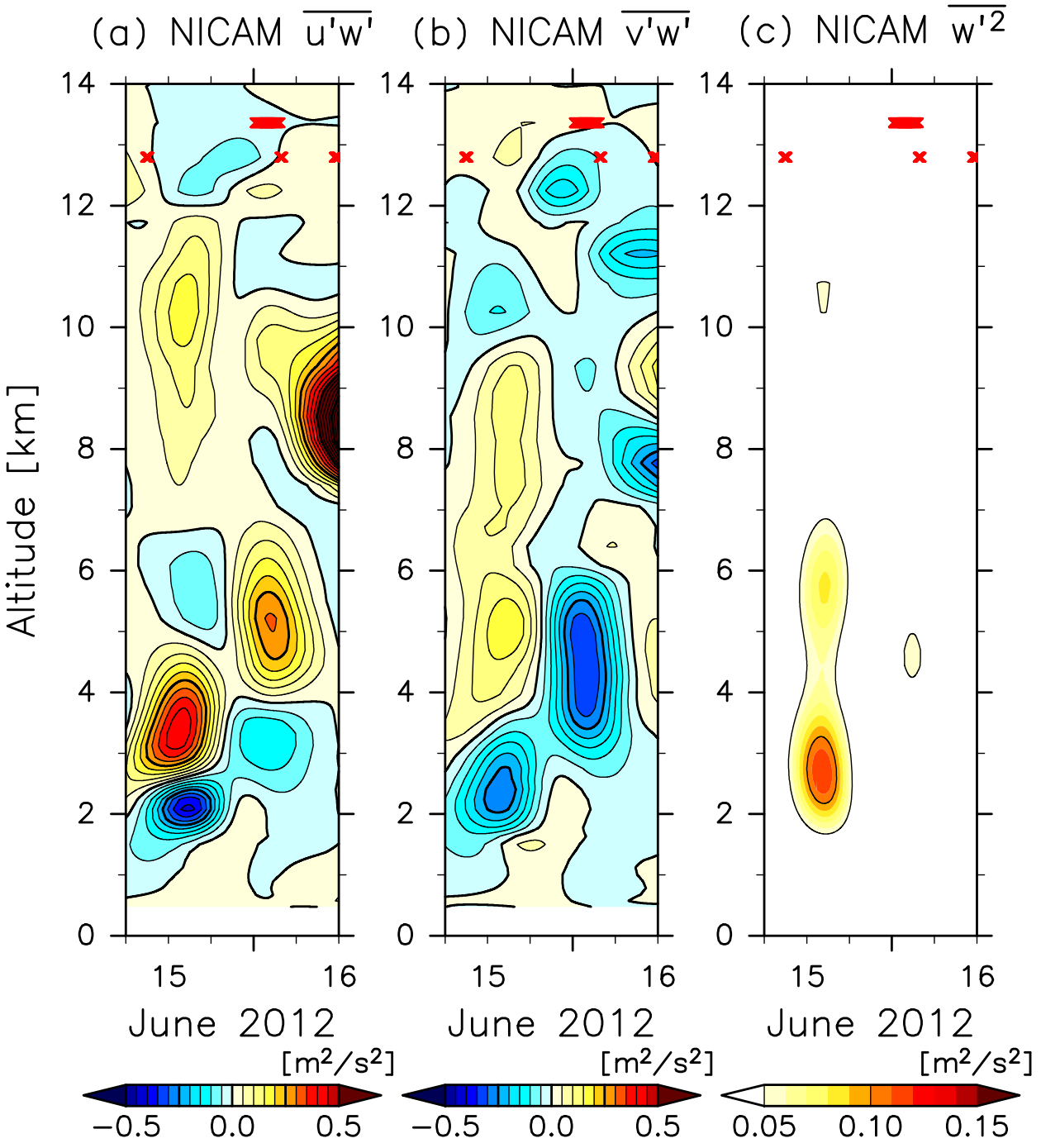

FIG. 13. As in Fig. 8, but for the NICAM data at 70.0°S, 40.0°E. Note that contour intervals are smaller than those of Fig. 8 by one order.

around 69°S, 50°E, which was located leeward of the mountain ridge along 54°E. On the other hand, a strong vertical wind was hardly seen over the ocean.

Strong northeasterly winds were observed along the altitude contours in Fig. 14. It is probably due to synoptic-scale cyclones off the coast as shown in Fig. 9. On the other hand, these cyclones showed an oval shape with isobaric lines along the coast rather than a circular shape. Such a shape of the cyclones could be affected by the Antarctic topography. To examine the effect of Antarctic topography on the horizontal wind, Fig. 15 shows the potential temperature, Froude number, and horizontal winds parallel to curves A and B in Fig. 14 at 1400 UTC 15 June 2012 in a latitude–altitude section along curve A. Whether

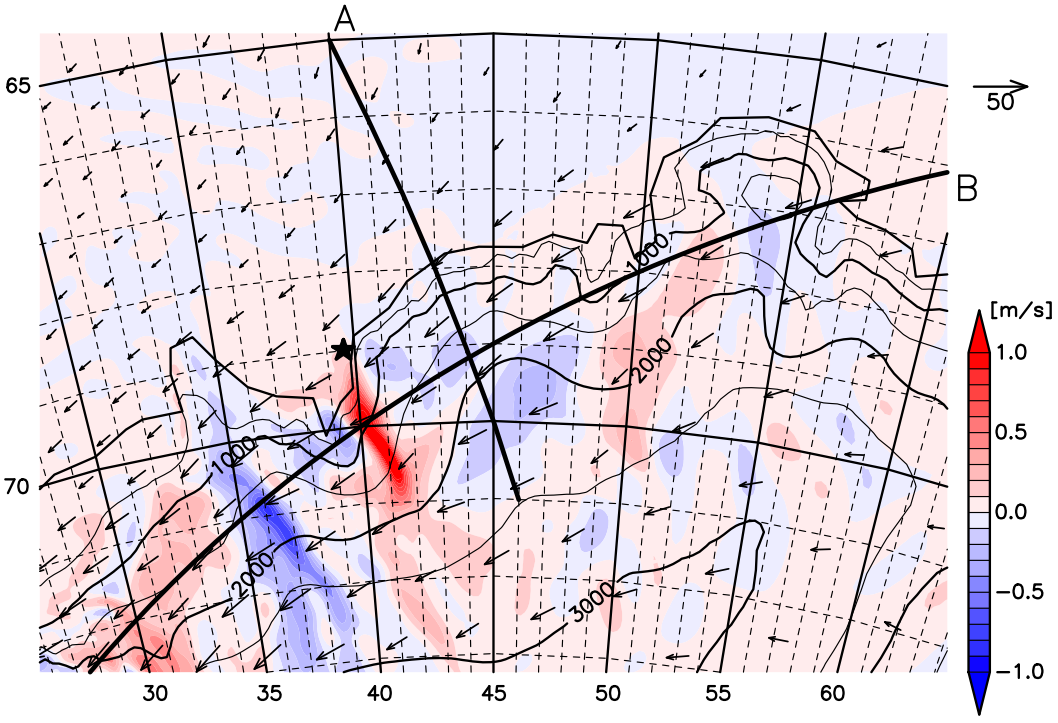

FIG. 14. Horizontal distributions of simulated vertical winds (colors) and horizontal winds (vectors) at an altitude of 5 km around Syowa Station at 1400 UTC 15 Jun 2012. Antarctic topography is shown by contours with contour intervals of 500 m. A star indicates a location of Syowa Station. Cross sections along curves A and B are shown in Figs. 15 and 16, respectively.

the flow will overpass the topography or be deflected around can be determined by the Froude number:

$$\mathrm{Fr} \equiv U\left(gH\frac{\Delta\theta}{\theta}\right)^{-0.5}, \qquad (1)$$

where U is the horizontal wind speed along curve B, g is the gravitational acceleration (9.8 m s^{-2}), H is the height of the obstacle (3 km), $\Delta\theta$ is the increase of potential temperature from the air parcel position to the top of the obstacle, and θ is the average potential temperature of the layer between the air parcel position and the top of the obstacle (Nigro et al. 2012). While the flow will overpass the topography for $\mathrm{Fr} \geq 1$, it will be forced around for $\mathrm{Fr} < 1$. The Froude number in Fig. 15b was smaller than unity almost everywhere. Since the synoptic-scale horizontal wind blew toward the coast above an altitude of 400 m (Fig. 15a), it is considered that the flow was forced around the topography in this altitude region. Such a horizontal wind toward the coast accumulated air mass along the slope of the topography (Fig. 15a) and enhanced a horizontal pressure gradient there. As a result, a horizontal wind along the topography was enhanced through the geostrophic balance and produced a maximum over 35 m s^{-1} at an altitude of 2.4 km around 69°S (Fig. 15b). Such a deflection and an intensification of horizontal wind along the topography are called a barrier effect (Steinhoff et al. 2008).

Figure 16 shows the Froude number, potential temperature, and on-plane wind vectors in a longitude–altitude section along curve B in Fig. 14. In this case, the Froude number is given as $\mathrm{Fr} \equiv U/NH$, where U and N are a horizontal wind velocity and a Brunt–Väisälä frequency at the air parcel position, respectively; and H is the characteristic depth of the flow. The variable H is defined roughly as the height of θ = 285-K contour in Fig. 16, which is assumed to be the interface between the topographically induced flow and the upper air (i.e., the isentropic surfaces above θ = 285 K look roughly flat, but those below θ = 285 K bend downward along the downslope of the mountain ridge at 40°–44°E in Fig. 16). While the Froude number was much smaller than unity over the ocean, it exceeded unity at an altitude of 2–2.5 km just above the mountain around 44°E where the horizontal wind speed near the surface was intensified. A strong upward wind was observed at an altitude of 2–9 km on its lee side, where the Froude number was close to unity. These features suggest that a near-surface horizontal wind was intensified and a hydraulic jump occurred on the lee side of the mountain ridge at 44°E in NICAM. In

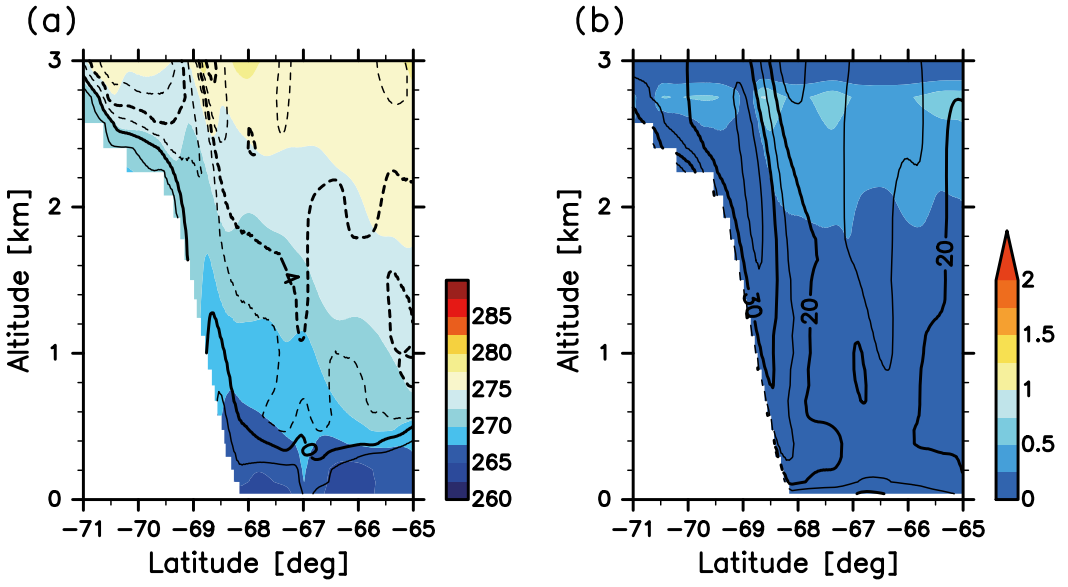

FIG. 15. Latitude–altitude sections along curve A in Fig. 14. (a) Potential temperature (colors) and horizontal wind parallel to curve A [contours; i.e., off-the-coast and to-the-coast winds are positive (solid) and negative (dashed), respectively], and (b) Froude number (colors) and horizontal wind parallel to curve B (contours; i.e., westward is positive) at 1400 UTC 15 Jun 2012. Contour intervals are (a) 2 and (b) 5 m s^{-1}.

addition, the hydraulic jump first appeared near the crest of the mountain ridge (70°S, 42°E) at 0200 UTC 15 June and moved leeward as the near-surface horizontal wind was intensified (not shown).

The NICAM simulation clearly demonstrated the occurrence of a hydraulic jump and strong upward wind on the lee side of mountain ridge near the Antarctic coast when cyclones approached Syowa Station. Since

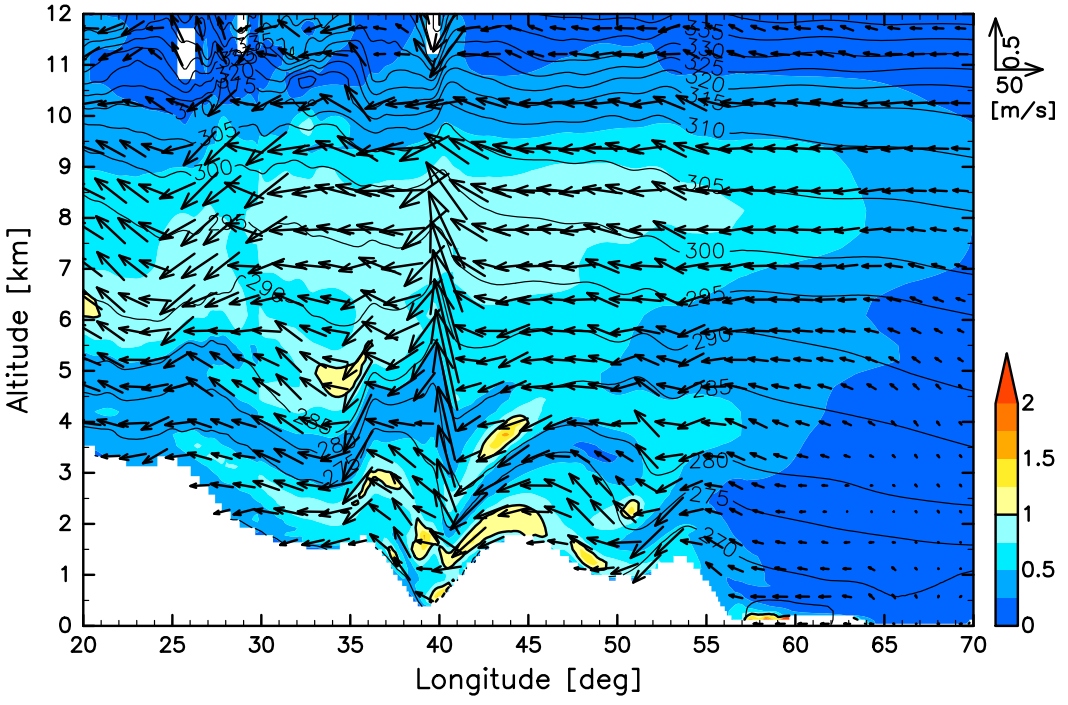

FIG. 16. Froude number (colors), potential temperature (contours), and on-plane wind vectors at 1400 UTC 15 Jun 2012 in a longitude–altitude section along curve B in Fig. 14. Contour intervals are 5 K. Contours of Fr = 1 are also plotted.

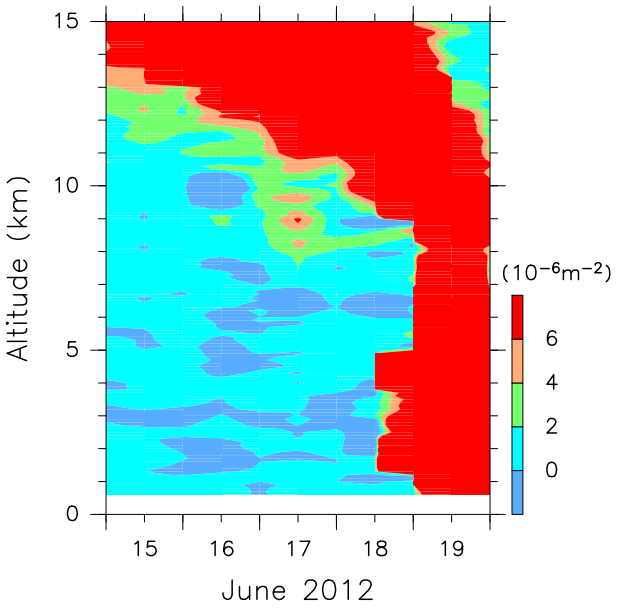

FIG. 17. Time–height section of the Scorer parameter computed with the radiosonde data at Syowa Station.

the strong VWDs observed by the PANSY radar at Syowa Station had a phase structure similar to those in NICAM and a location of the hydraulic jump can move in response to the strength of near-surface wind, the observed VWDs are possibly due to such hydraulic jump. Another possibility is that they were due to lee waves, which have a standing phase structure, large amplitudes, and little vertical flux of horizontal momentum. To confirm the possibility of lee waves, Fig. 17 shows a time–height section of the Scorer parameter computed by the radiosonde data at Syowa Station and running averaged for 1 km in the vertical. The Scorer parameter is defined as

$$l^2 \equiv \frac{N^2}{U^2} - \frac{U_{zz}}{U}, \tag{2}$$

where U is the horizontal wind velocity parallel to the surface wind. Here the surface wind direction is assumed to be 60° (i.e., from east-northeast) from Fig. 11. Taking k as a horizontal wavenumber of the topographically forced gravity wave, the gravity wave can vertically propagate where $l^2 > k^2$. On the other hand, if the Scorer parameter decreases sharply with height and $l^2 - k^2$ changes its sign from positive to negative across a certain height, the gravity wave can be trapped below the height of $l^2 = k^2$ and become a lee wave (Scorer 1949). The Scorer parameter in Fig. 17 does not show a large variation below an altitude of 10 km and sharply increases between altitudes of 10 and 15 km during 16–17 June 2012. This result suggests that the VWDs observed during 16–17 June 2012 were not due to the lee waves but due to the hydraulic jump. On the other hand, the Scorer parameter was enhanced in an altitude region of 1–5 km at 1200 UTC 18 June 2012, which implies that the VWD observed around 1200 UTC 18 June 2012 might be due to a lee wave.

7. Summary and conclusions

Vertical wind disturbances (VWDs) during a strong wind event (SWE) at Syowa Station (69.0°S, 39.6°E) in the Antarctic were examined using MST radar observations and a high-resolution numerical simulation in detail. We focused on a VWD event in the troposphere observed by the PANSY radar, which is the first MST/IS radar in the Antarctic, at Syowa Station during 15–19 June 2012. During this time period, two synoptic-scale cyclones approached Syowa Station and were located to its north. A barrier effect enhanced a surface pressure gradient around Syowa Station in association with the southerly flow due to these cyclones above the ocean and caused a strong northeasterly or easterly wind at the surface, which is called a SWE.

The VWDs observed by the PANSY radar during the SWE had a nearly standing phase structure in the troposphere and a frequency power spectrum proportional to $\omega^{-5/3}$. On the other hand, it seemed that the strong VWDs observed around 0000 UTC 17 June, 1400 UTC 17 June, and 1200 UTC 18 June 2012 were not associated with systematic horizontal momentum fluxes ($\overline{u'w'}$ and $\overline{v'w'}$) regardless of their large amplitudes.

To examine meteorological fields around Syowa Station and VWDs during the SWE, we carried out a numerical simulation using the Nonhydrostatic Icosahedral Atmospheric Model (NICAM), in which horizontal grids are finer near Syowa Station than other regions to reproduce both the synoptic-scale and mesoscale phenomena saving computational cost. Two cyclones approaching Syowa Station and synoptic-scale meteorological fields during the SWE were reproduced well by NICAM. A strong VWD event was also simulated by NICAM at 70.0°S, 40.0°E, which was located to the south of Syowa Station by 120 km. During this VWD event, the near-surface wind around 70.0°S, 40.0°E was intensified by a barrier effect as well as synoptic-scale cyclones. In addition, NICAM clearly demonstrated that the VWD at 70.0°S, 40.0°E was due to a hydraulic jump on the lee side of the coastal mountain ridge.

The Scorer parameter computed by the radiosonde data at Syowa Station indicated that the VWDs observed during 16–17 June 2012 were not due to the lee waves but likely due to the hydraulic jump similar to that in NICAM. On the other hand, a possibility of the lee

wave was also suggested as a mechanism of the VWD observed on 18 June 2012. This result is in contrast to the results of Valkonen et al. (2010) and Arnault and Kirkwood (2012), which observed the VWDs induced by vertically propagating mountain waves with the MARA radar near Aboa/Wasa Station (73.0°S, 13.4°W).

Most of the Antarctic coastal region is exposed to strong surface winds induced by the katabatic forcing and cyclones from the Southern Ocean storm track. They can excite many kinds of mesoscale phenomena including a hydraulic jump and lee waves discussed in this paper. However, how frequent each of them is excited over Antarctica and how large their impact on the Antarctic atmosphere and climate is are still not sufficiently understood because of a lack of observations in the Antarctic. The PANSY radar is one of a few instruments to accurately measure both the horizontal and vertical winds with high temporal and vertical resolutions in the troposphere and lower stratosphere in the Antarctic. By continuing the observation and accumulating the data, the PANSY radar will significantly contribute to understanding how mesoscale phenomena such as VWDs are caused in the Antarctic and how much they impact the stratosphere, mesosphere, and thermosphere through momentum and energy transport.

Acknowledgments. The operational observations of surface meteorology and the PANSY radar at Syowa Station were conducted by the Japanese Antarctic Research Expedition (JARE). The surface meteorological data at Syowa Station were provided by the Japan Meteorological Agency. The authors appreciate constructive and useful comments from Prof. M. Satoh at the Atmosphere and Ocean Research Institute (AORI) about NICAM. The authors are deeply grateful to Prof. Niino at AORI for his insightful comments and suggestions. We are also indebted to Assist. Prof. N. Hirasawa at the National Institute of Polar Research (NIPR) for his kindly providing AVHRR data. This study is supported by Grant-in-Aid for Scientific Research (A) 25247075 of the Ministry of Education, Culture, Sports and Technology, Japan. Numerical simulations were run on the supercomputer at NIPR. The MERRA data were provided by the NASA GSFC Global Modeling and Assimilation Office (GMAO) at http://disc.sci.gsfc.nasa.gov/daac-bin/DataHoldings.pl. Figures were drawn using Dennou Club Library (DCL). The production of this paper was supported by an NIPR publication subsidy.

REFERENCES

Adams, N., 2004: A numerical modeling study of the weather in East Antarctica and the surrounding Southern Ocean. *Wea. Forecasting,* **19,** 653–672, doi:10.1175/1520-0434(2004)019<0653:ANMSOT>2.0.CO;2.

Arnault, J., and S. Kirkwood, 2012: Dynamical influence of gravity waves generated by the Vestfjella Mountains in Antarctica: Radar observations, fine-scale modelling and kinetic energy budget analysis. *Tellus,* **64A,** 17261, doi:10.3402/tellusa.v64i0.17261.

Blackman, R. B., and J. W. Tukey, 1958: *The Measurement of Power Spectra from the Point of view of Communication Engineering.* Dover Publications, 190 pp.

Ecklund, W. L., B. B. Balsley, D. A. Carter, A. C. Riddle, M. Crochet, and R. Garello, 1985: Observations of vertical motions in the troposphere and lower stratosphere using three closely spaced ST radars. *Radio Sci.,* **20,** 1196–1206, doi:10.1029/RS020i006p01196.

——, K. S. Gage, G. D. Nastrom, and B. B. Balsley, 1986: A preliminary climatology of the spectrum of vertical velocity observed by clear-air Doppler radar. *J. Climate Appl. Meteor.,* **25,** 885–892, doi:10.1175/1520-0450(1986)025<0885:APCOTS>2.0.CO;2.

Fudeyasu, H., Y. Wang, M. Satoh, T. Nasuno, H. Miura, and W. Yanase, 2008: Global cloud-system-resolving model NICAM successfully simulated the lifecycles of two real tropical cyclones. *Geophys. Res. Lett.,* **35,** L22808, doi:10.1029/2008GL036003.

King, J. C., and J. Turner, 1997: *Antarctic Meteorology and Climatology.* Cambridge University Press, 409 pp.

Lin, Y. L., R. D. Farley, and H. D. Orville, 1983: Bulk parameterization of the snow field in a cloud model. *J. Climate Appl. Meteor.,* **22,** 1065–1092, doi:10.1175/1520-0450(1983)022<1065:BPOTSF>2.0.CO;2.

Miura, H., M. Satoh, T. Nasuno, A. T. Noda, and K. Oouchi, 2007: A Madden–Julian Oscillation event simulated using a global cloud-resolving model. *Science,* **318,** 1763–1765, doi:10.1126/science.1148443.

Nakanishi, M., and H. Niino, 2004: An improved Mellor–Yamada level-3 model with condensation physics: Its design and verification. *Bound.-Layer Meteor.,* **112,** 1–31, doi:10.1023/B:BOUN.0000020164.04146.98.

Nigro, M. A., J. J. Cassano, M. A. Lazzara, and L. M. Keller, 2012: Case study of a barrier wind corner jet off the coast of the Prince Olav Mountains, Antarctica. *Mon. Wea. Rev.,* **140,** 2044–2063, doi:10.1175/MWR-D-11-00261.1.

Parish, T. R., and D. H. Bromwich, 1987: The surface windfield over the Antarctic ice sheets. *Nature,* **328,** 51–54, doi:10.1038/328051a0.

Rienecker, M., and Coauthors, 2011: MERRA: NASA's Modern-Era Retrospective Analysis for Research and Applications. *J. Climate,* **24,** 3624–3648, doi:10.1175/JCLI-D-11-00015.1.

Sato, K., 1990: Vertical wind disturbances in the troposphere and lower stratosphere observed by the MU radar. *J. Atmos. Sci.,* **47,** 2803–2817, doi:10.1175/1520-0469(1990)047<2803:VWDITT>2.0.CO;2.

——, and N. Hirasawa, 2007: Statistics of Antarctic surface meteorology based on hourly data in 1957-2007 at Syowa Station. *Polar Sci.,* **1,** 1–15, doi:10.1016/j.polar.2007.05.001.

——, and Coauthors, 2014: Program of the Antarctic Syowa MST/IS Radar (PANSY). *J. Atmos. Sol.-Terr. Phys.,* **118A,** 2–15, doi:10.1016/j.jastp.2013.08.022.

Satoh, M., T. Matsuno, H. Tomita, H. Miura, T. Nasuno, and S. Iga, 2008: Nonhydrostatic icosahedral atmospheric model (NICAM) for global cloud resolving simulations. *J. Comput. Phys.,* **227,** 3486–3514, doi:10.1016/j.jcp.2007.02.006.

Scorer, R., 1949: Theory of waves in the lee of mountains. *Quart. J. Roy. Meteor. Soc.,* **75,** 41–56, doi:10.1002/qj.49707532308.

Steinhoff, D. F., D. H. Bromwich, M. Lambertson, S. L. Knuth, and M. A. Lazzara, 2008: A dynamical investigation of the May 2004 McMurdo Antarctica severe wind event using AMPS. *Mon. Wea. Rev.,* **136,** 7–26, doi:10.1175/2007MWR1999.1.

Tomita, H., 2008a: A stretched grid on a sphere by new grid transformation. *J. Meteor. Soc. Japan,* **86,** 107–119, doi:10.2151/jmsj.86A.107.

——, 2008b: New microphysics with five and six categories with diagnostic generation of cloud ice. *J. Meteor. Soc. Japan,* **86,** 121–142, doi:10.2151/jmsj.86A.121.

Trenberth, K. E., 1991: Storm tracks in the Southern Hemisphere. *J. Atmos. Sci.,* **48,** 2159–2178, doi:10.1175/1520-0469(1991)048<2159:STITSH>2.0.CO;2.

Turner, J., T. A. Lachlan-Cope, G. J. Marshall, S. Pendlebury, and N. Adams, 2001: An extreme wind event at Casey Station, Antarctica. *J. Geophys. Res.,* **106,** 7291–7311, doi:10.1029/2000JD900544.

——, S. N. Chenoli, A. Samah, G. Marshall, T. Phillips, and A. Orr, 2009: Strong wind events in the Antarctic. *J. Geophys. Res.,* **114,** D18103, doi:10.1029/2008JD011642.

Valkonen, T., T. Vihma, S. Kirkwood, and M. M. Johansson, 2010: Fine-scale model simulation of gravity waves generated by Basen nunatak in Antarctica. *Tellus,* **62A,** 319–332, doi:10.1111/j.1600-0870.2010.00443.x.

Vincent, R. A., and I. M. Reid, 1983: HF Doppler measurements of mesospheric gravity wave momentum fluxes. *J. Atmos. Sci.,* **40,** 1321–1333, doi:10.1175/1520-0469(1983)040<1321:HDMOMG>2.0.CO;2.

WMO, 1957: Meteorology—A three-dimensional science. *WMO Bull.,* **6,** 134–138.